PHILOSOPHICAL TRANSACTIONS OF THE ROYAL SOCIETY A MATHEMATICAL, PHYSICAL & ENGINEERING SCIENCES

Studies in Hydrodynamic Thrust Bearings. II. Comparison of Calculated and Measured Performance of Tilting Pads by means of Interferometry

C. L. Robinson and A. Cameron

Phil. Trans. R. Soc. Lond. A 1975 **278**, 367-384
doi: 10.1098/rsta.1975.0030

Phil. Trans. R. Soc. Lond. A. **278**, 367–384 (1975) [367]
Printed in Great Britain

STUDIES IN HYDRODYNAMIC THRUST BEARINGS

II. COMPARISON OF CALCULATED AND MEASURED PERFORMANCE OF TILTING PADS BY MEANS OF INTERFEROMETRY

By C. L. Robinson and A. Cameron
Lubrication Laboratory, Department of Mechanical Engineering, Imperial College of Science and Technology, London S.W. 7

(*Communicated by H. Ford, F.R.S. – Received* 23 *April* 1974)

[Plates 14 and 15]

CONTENTS

In this novel use of interferometry the film shape of a thrust bearing can be determined to a very high degree of accuracy by making the runner of glass and coating it with a semi-reflecting chrome layer. The runner is loaded by a hydrostatic bearing immediately above the experimental pad. By making the chamber of the hydrostatic recess of glass and by using the fact that glass and oil have almost the same refractive index, fringes between the tilting pad and the chrome layer can be obtained. The heat conduction through the pad was found to be important.

The agreement between the experimental film shape and that calculated in part I is surprisingly good. It is only the very complete map of the film shape that allows the detailed comparison of theory and experiment to be made.

Nomenclature

B	pad width	V	fringe visibility
h	film thickness	α	beam intensity ratio
h_0	minimum film thickness	δ	distortion
k	thermal conductivity of pad	η	average film viscosity
L	coherence length	λ	wavelength
n	refractive index	ρ	lubricant density
N	rotational speed of collar	σ	lubricant specific heat
p_s	pad specific load	ψ	half angle subtended by light source at lens centre
t	pad thickness		
U	mean sliding speed		

Introduction

In the preceding part the theory of bearing distortion, both elastic and thermal was developed. In this part the method by which distortions were measured are described and the results compared with theory.

Experimental method

The requirement is to measure the variation of oil film thickness over the entire thrust pad. Interferometry is ideally suited to this task but of course one of the frictional members must be made from a transparent material. The runner was chosen because (i) it is easier to load and also (ii) the runner remains more nearly isothermal than the pad. Therefore, the difference in thermal properties of glass compared with those of the steel/bearing metal pad combination are not so serious.

Glass is a very poor bearing material but when it is given a semi-reflecting coating – in our case chromium – this in part disappears as the system behaves as if it were bearing metal–oil–chromium rather than bearing metal–oil–glass.

In this section the mechanical part of the test apparatus will first be described. Next the optics will be discussed in some detail. While most of the optical data is relatively standard, it is not a subject with which engineers are normally familiar. Furthermore much of the data assembled here is somewhat scattered as very few optical interference systems operate in oil.

Principles of interferometry

What is so valuable about the use of interferometry is that with oil as the fluid, separation between each fringe (with mercury green light) is 0.184 μm; the sensitivity is, therefore, more than

adequate. The disadvantage of using monochromatic light is that it only gives *changes* of film thickness. To obtain absolute values in the thickness range of 2.54–25.4 μm two or more colours have to be used, which is troublesome. Another method is to use fringes of equal chromatic order which requires (in its classical form) a spectrometer giving a line-by-line picture. An alternative which is now being developed in the laboratory is to take white light interferograms, then use narrow pass Balzar filters to obtain a series of monochromatic interference patterns. While at the start of the work these various techniques were discussed, as the study progressed such refinements were seen to be unnecessary.

The basic principles of interferometry have been known since Newton's *Optiks* of 1704.

The main consideration in designing a system is that the fringe visibility should be maximum. This comes about when the two interfering rays are of the same intensity. If one ray has an intensity I and the other αI, the fringe visibility V is given by $V = 2\sqrt{\alpha}/(1+\alpha)$. V is only weakly dependent on α up to quite large values. At $\alpha = \frac{1}{2}$, $V = 0.94$, and at $\alpha = \frac{1}{4}$, $V = 0.8$. The requirement for equal intensity of the two rays, therefore, is not critical.

Coherence length is a most important factor in interferometry. It defines the mean length for which any given bundle of rays are in phase. If the optical path length between the interfering surfaces is much greater than the coherence length then no interference will occur. Born & Wolf (1965) gave the following approximate formula for coherence length: $L = \lambda^2/\Delta\lambda$ where λ is the mean wavelength of the source and $\Delta\lambda$ is the band width at half peak intensity. The source used had a wavelength of 0.5461 μm (mercury green) and a half peak band width of 0.006 μm. This gives a coherence length of *ca.* 50 μm. The thickest film to be measured is approximately 25 μm so the coherence length should suffice.

Next the angle of collimation must be considered. Françon (1966) considered the effects of non-parallel light due to a finite source size on fringe visibility. If ψ is the half angle subtended by the source at the centre of the collimating lens then visibility is

$$V = (\sin m)/m, \quad \text{where} \quad m = \pi h\psi^2/n\lambda$$

and h is the distance between reflecting surfaces in a medium of refractive index n. For $V = 0.95$ and $h/\lambda = 50$ (max.), ψ must not exceed 79 mrad. The source used here had a width of 0.2 mm and the focal length of the collimating lens was 100 mm so ψ is in fact 1 mrad.

Reflecting surfaces

First the peak to valley roughness of the reflecting surfaces must not change a fringe from bright to dark. This means it must be less than $\lambda/4n$ for mercury green and oil, this is [0.5461/(4 × 1.5)] equal to 0.091 μm. In practice it had been found that if the surfaces have a roughness of 0.025 μm c.l.a. or better this is satisfactory.

Originally, standard mild steel thrust pads having a tin based white metal surface were polished using a ground glass lapping plate. Although a sufficiently reflective surface was obtained and some interesting results were produced, white metal was found unsuitable as an interferometric surface as will be discussed later. Stainless steel pads were used as an alternative and these were lapped and polished to a roughness better than 0.013 μm c.l.a. and an overall flatness of 0.13 μm.

The reflectivity of the pads and of the chromium semi-reflecting layer had next to be matched.

For the pads reflectivities were measured in air and oil by comparing them with known

reflectivities of a silver plate, using a constant light source and a photocell. The results were tabulated.

For good visibility the intensity of the two interfering beams must be similar. In figure 1 let an incident ray of unit intensity strike the semi-reflecting layer. It is split into two beams. One is reflected at the chromium/oil interface with an intensity of R_{cr}. The remaining part continues, some is absorbed and the transmitted portion has an intensity T_{cr}. At the steel oil surface, whose reflectivity is R_{steel}, this is now reflected and has an intensity of $(R_{steel} T_{cr})$. The part that continues through the semi-reflecting chromium of intensity $(R_{steel} T_{cr}^2)$ will interfere with the first reflected ray. For their intensities to be the same R_{cr} must equal $(R_{steel} T_{cr}^2)$.

TABLE 1. REFLECTIVITIES OF METAL SURFACES

surface	in air	in oil	ratio, oil/air
white metal tilting pad	0.25	0.20	0.8
stainless steel tilting pad	0.30	0.26	0.87
stainless steel fixed pad	0.56	0.48	0.86

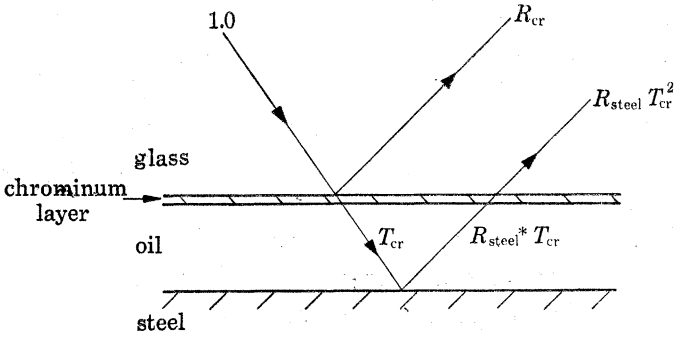

FIGURE 1. Intensities of interfering rays.

Ellsworth (1968) gave some data for the properties of thin chromium films, which though fragmentary are sufficient for design purposes. First the reflectivity ratio of air to oil is about 1.66, secondly transmission ratio of air to oil is 0.8 and thirdly for a chrome film in oil when $R = 0.16$, $T = \frac{1}{2}$, and obviously when $R = 0$, $T = 1$. Assuming then a linear relation between R and T the equality $R_{cr} = R_{steel} T_{cr}^2$ can be satisfied. For $R_{steel} = 0.25$, $R_{cr} = 0.10$ and for $R_{steel} = 0.5$, $R_{cr} = 0.14$. When chromium is being deposited the reflectivities are monitored *in vacuo* which can be taken as being equal to those in air. Hence a reflectivity of the chrome layer in air should be specified as 1.66 times the required reflectivity in oil, i.e. between 16.6 and 23 % for R_{steel} between 0.25 and 0.5. As shown earlier this is not very critical and as the reflectivity of the pad tends to drop with use, a value about 19 or 20 % was found suitable.

This point has been dealt with at some length as it is not found in any of the standard textbooks on interferometry.

Since only the changes in shape of the film are considered the vexed question of phase shift on reflexion does not enter the discussion. Concerning the other pieces of equipment, these were mostly standard. The beam splitter was a 50 mm square glass plate with a 50/50 vacuum deposited layer of TiO_2 and the camera an Asahi Pentax 35 mm with an $f/3.8$, 135 mm lens. The exposure normally was 1 ms with Ilford HP4 film having an A.S.A. rating of 500 when used with a fine grain developer.

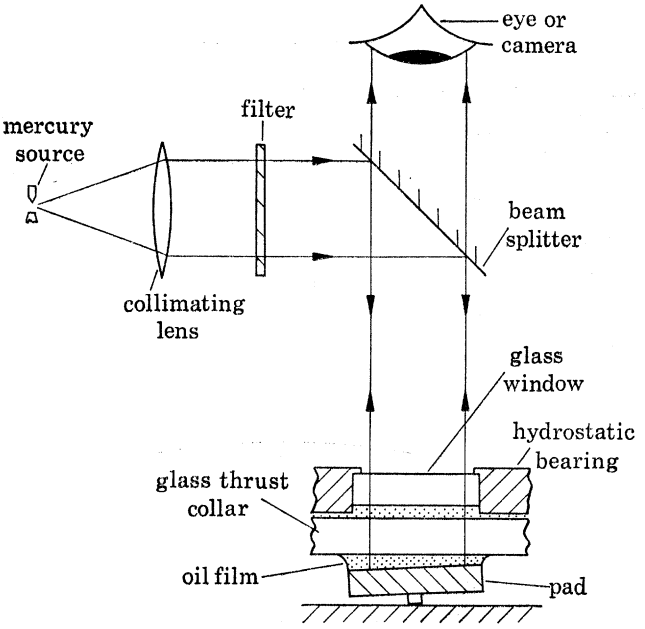

FIGURE 2. Schematic view of test system.

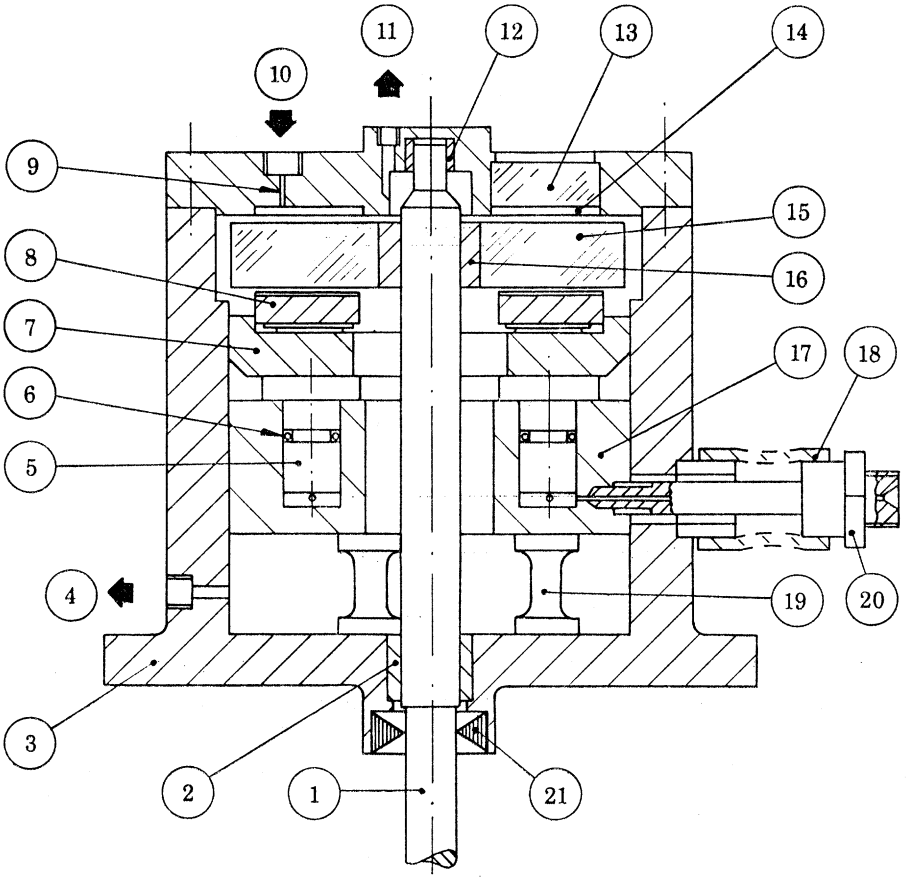

FIGURE 3. Section of test head. 1, Shaft; 2, PTFE bush; 3, bearing housing; 4, oil outlet; 5, loading piston; 6, 'O' ring seal; 7, bearing carrier ring; 8, thrust pad; 9, capillary restrictor; 10, oil inlet; 11, oil outlet; 12, PTFE bush; 13, glass window; 14, hydrostatic bearing recess; 15, glass thrust collar; 16, rubber bush; 17, monobloc loading cylinder assembly; 18, flexible tubing; 19, strain gauge load cell; 20, pressure inlet for loading device; 21, oil seal.

Mechanical design

The basic idea behind the test machine is to load a 76 mm diameter thrust ring of 3 pads against a rotating glass plate. The working face of the glass is semi-reflecting and one of the pad surfaces is highly polished so interference fringes can be generated. The loading device is an array of six pressurized pistons below the thrust pad carrier ring. The reaction of the glass runner is taken by a hydrostatic thrust bearing containing three glass windows.

A schematic view of the system is shown in figure 2. Interference patterns are produced between the chrome layer on the glass thrust collar and the pad surface. Figure 3 shows the overall section of the test head which allows the various parts to be identified.

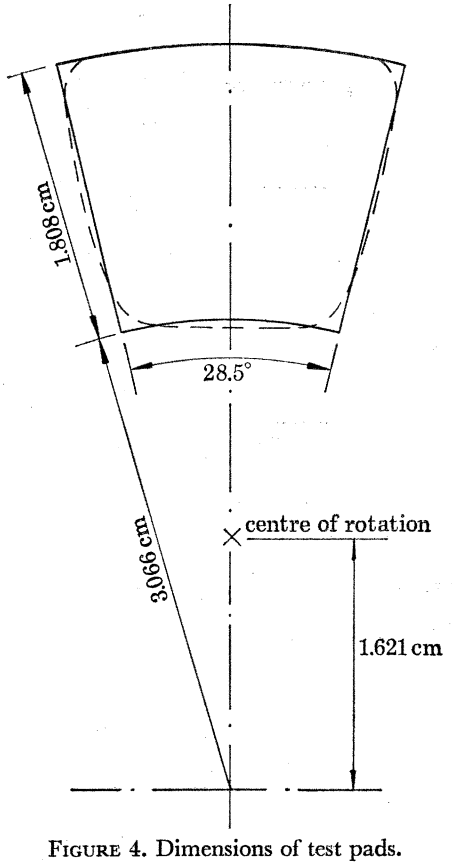

FIGURE 4. Dimensions of test pads.

Tilting pad bearing

The bearing was a standard 76 mm diameter unit normally having six pads. Only three of the six were used, ensuring equal loading. The pads are supported centrally by a line pivot of 10 % of the mean circumferential width and half the mean radial extent. The dimensions of the pad are shown dotted in figure 4 which was approximated by a geometrically simpler sector, given as a full line for the purposes of mathematical analysis.

Glass disk

The glass disk was of 13 mm thick plate glass. Simple calculations showed that the bending stresses would not exceed 6.9 MN/m². under the experimental conditions. The surfaces were flat

to within half a light fringe and parallel to within 5 fringes (1.4 μm). The disk was mounted on the shaft with a spacing bush of nitrile rubber glued with cyanoacrylate cement to allow a flexible drive, thus eliminating any swashing action.

Hydrostatic bearing

Owing to its low tensile strength, the glass runner was supported over as large an area as possible by a hydrostatic backing bearing fitted with glass windows allowing an unobscured view of the pads. The windows were cemented into milled recesses by araldite epoxy resin.

The dimensions of the recesses were calculated from Rippel (1962). At maximum loading and a standard oil flow of 76 cm^3/s the recess pressure was 1.93 MN/m^2 and the film thickness 0.1 mm.

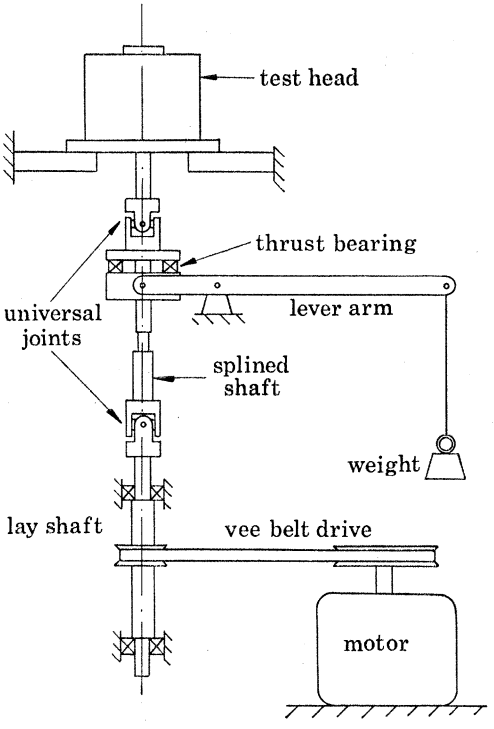

FIGURE 5. Drive transmission and jacking device.

Loading

The load was applied by six pistons of 11 mm diameter located on the mean p.c.d. of the bearing and were fitted with 'O' ring seals. This naturally involved an uncertain amount of friction, so the true load was measured by three tubular load cells of 6.4 mm diameter and of 0.5 mm wall thickness. A load of 6.7 kN produced a strain over the gauge length of 0.1 %. Two foil strain guages of the self temperature compensating type were fixed at the ends of a diameter to each cell. Connecting them in series eliminated any response to bending.

The stainless steel pads had very poor lubricating quality so on start up a jacking device was fitted to give a positive clearance between runner and pads. This comprised a forked lever arm and small ball thrust bearing, similar to a car clutch release (figure 5). There is, of course, always a film between the collar and the hydrostatic bearing when it is pressurized.

Oil circuit and lubricant

The oil system is standard. A 35 MN/m², 152 cm³/s pump supplies the hydrostatic bearing through a 2.5 μm filter and a 1.1 dm³ hydraulic accumulator minimizes pressure fluctuations. The thrust collar is lubricated from the bearing spill, which returns via an oil cooler to a 18 dm³ sump. The oil used throughout was an s.a.e. 30 with anti-oxidant and anti-scuffing agents and a dispersant. Its properties are listed in table 2.

TABLE 2. MINERAL OIL PROPERTIES

mineral oil s.a.e. 30	311 K	339 K	367 K
viscosity/m² s⁻¹	1.05	0.32	0.13
specific heat/J kg⁻¹ K⁻¹	1830	1960	2080
density/kg m⁻³	866	850	830
thermal conductivity/W m⁻¹K⁻¹	0.137	0.135	0.133

Instrumentation

Bearing speed was measured by a 60 tooth wheel and magnetic pick up feeding a digital counter.

For temperature measurements nine thermocouples were installed 0.76 mm from the pad surface. A 0.94 mm diameter flat bottomed hole was drilled and a ceramic sleeve inserted. Chrome–alumel wire (40 s.w.g.) was stripped of its insulation 25 mm from the end and fed into the insulator till the ends touched the hole bottom. A capacitor was discharged across the other ends of the conductors which welded them in place. Their leads were then secured by araldite epoxy resin.

Further thermocouples were placed in the bearing grooves. The temperatures were read on an electronic millivoltmeter calibrated in degrees centigrade. The accuracy is estimated at ± 1 K.

Pad load was recorded by a standard d.c. strain gauge bridge.

RESULTS

White metal faced pads

The first tests were carried out by using a commercial pad with a thin layer of tin based white metal lapped to 0.26 μm flatness and polished to 0.026 μm c.l.a. Running at 2.76 MN/m² specific load and speeds of 209, 419 and 628 rad/s gave surprising results. At 209 rad/s the film shape is clear (figure 6 *a*, plate 14) but the fringes are somewhat blurred at the exit. In all pictures entry is at the left and exit at the right. At 419 rad/s (figure 6 *b*) the bands are clear at entry but become progressively blurred at exit. At 628 rad/s the film shape (figure 6 *c*) is completely obscured and no information can be obtained.

This roughening was attributed to anisotropic expansion of the tin and antimony which are the major constituents of the white metal used. The change between successive dark fringes is 0.184 μm, the white metal is 0.51 mm thick and a tin has anisotropic thermal expansions of 24×10^{-6}/K and 12×10^{-6}/K. A temperature rise of 29 K would, therefore, account for the shift and this was measured.

This differential expansion has been suspected but never seen till these interference pictures demonstrated its existence.

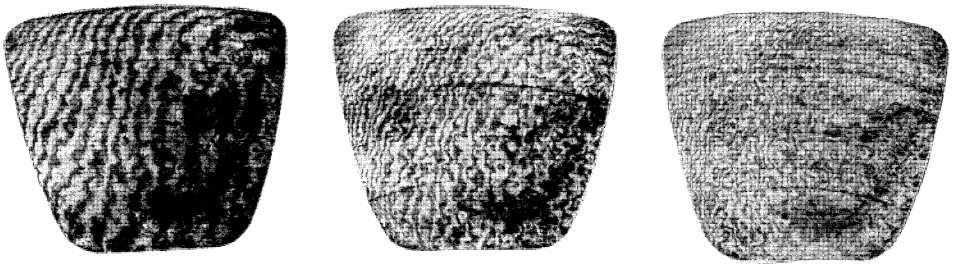

(*a*) 209 rad/s (*b*) 419 rad/s (*c*) 628 rad/s

FIGURE 6. Fringes from white metal pad at 2.76 MN/m² specific load.

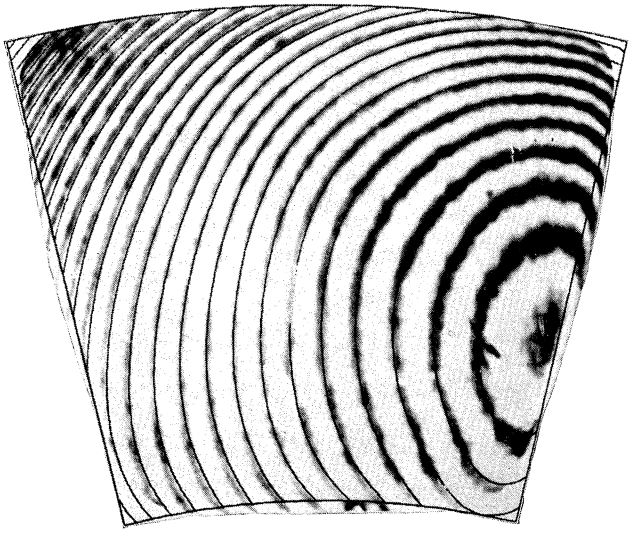

FIGURE 7. Typical interferogram with digital print out superimposed.

(*Facing p.* 374)

PHILOSOPHICAL TRANSACTIONS OF THE ROYAL SOCIETY A MATHEMATICAL, PHYSICAL & ENGINEERING SCIENCES

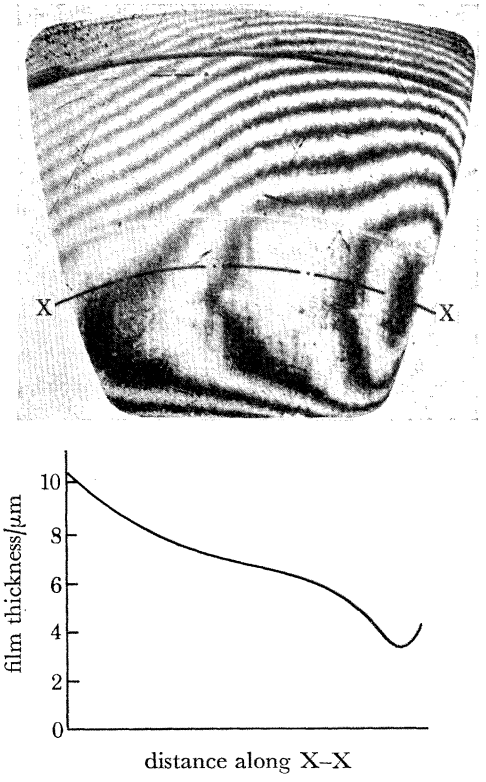

FIGURE 9. Interferogram and cross section showing ehl construction at exit.

PHILOSOPHICAL TRANSACTIONS OF THE ROYAL SOCIETY A MATHEMATICAL, PHYSICAL & ENGINEERING SCIENCES

Stainless steel pads: test procedure

To overcome the difficulties experienced with whitemetal the experimental pad was machined from stainless steel (EN58B). The other two pads were standard white metal faced, as the lubricating quality of EN58B is not good. Once the jacking device was installed few problems were encountered with scratching, which had till then given great trouble. At all times cleaning was found to be vital. The bearing components were cleaned ultrasonically for 10–15 min in toluene and washed with acetone just before assembly.

Before taking readings the machine was run with the surfaces jacked apart for 30 min under full oil flow. Some slight scratching still occurred on loading, but did not affect the clarity of the interferograms. The relevant properties of EN58B are listed in table 3.

TABLE 3. PROPERTIES OF EN58B

Young modulus/MN m^{-2}	0.193×10^6
coefficient linear expansion/K^{-1}	17×10^{-6}
thermal conductivity/W m^{-1} K^{-1}	25.0
Poisson ratio	0.294

All tests were conducted with a constant oil flow to the housing of 82 cm^3/s and inlet temperature of 313 K. The easiest way of ensuring this flow was to arrange for a pressure drop of 2.76 MN/m across the filter. At start and stop the flow was checked by timing the filling of a 4 dm^3 container directly.

After start up the thermocouple readings became steady after 1 min, but a further 2 were allowed to ensure no transient effects were present. The ten thermocouples readings, load and speed were logged and a photograph of the fringes taken. Less than 30 s were needed to do this.

Readings were taken at specific loads of 1.37, 2.76, 4.14, 5.52, 6.89 MN/m^2 and at nominal speeds of 157, 209, 314, 419, 523 and 628 rad/s. Loads of 5.52 and 6.89 MN/m^2 were not run at 157 rad/s for fear of scuffing.

Film shape

A typical photograph of interference fringes is shown in figure 7, plate 14. This is a contour map where each successive black fringe represents a film thickness change of 0.184 μm. This was converted to numerical data by placing a 9×9 grid over the photograph and noting the fringe order at each of the 81 nodal points. The black fringe showing the minimum film being designated the order 1.

To check the adequacy of these 81 nodes to describe the film shape, a computer program developed by Munro (1967) was used to reproduce the contours with an off-line digital plotter. The dark lines superimposed on the fringes in figure 7 are the contours taken from the digital plotter. The triangle is fringe no. 1, or the minimum film thickness and the agreement is excellent.

In all subsequent plots these digital print outs will be used, rather than actual photographs. In these plots, contours are at 0.26 μm intervals, inlet on the right and exit on the left. In figure 8, typical film thickness results are shown. They are all drawn by the digital plotter and compared with theoretical contours. At low speeds and loads, e.g. 161 rad/s and 1.37 MN/m^2 the shape is not a great departure from a wedge between flat surfaces as one would expect with a flat pad and line pivot. As the speed increases distortion, especially thermal distortion, gets larger, particularly over the trailing part of the pad. At 314 rad/s and above the film shapes are similar and vary only in magnitude.

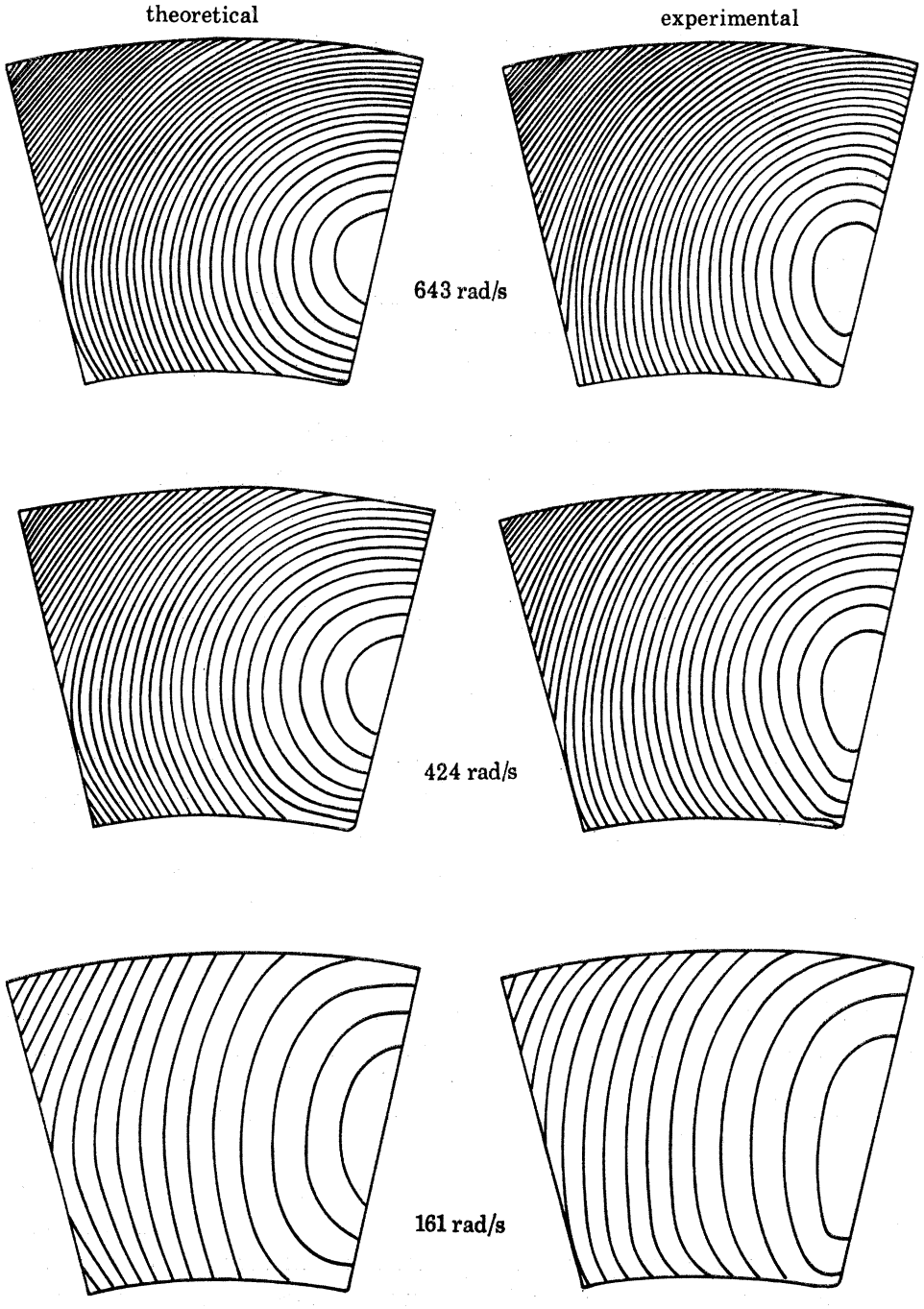

FIGURE 8*a*. For description see opposite.

At low speed and high load, e.g. 213 rad/s and 6.89 MN/m², a film showing the classical ehl-type construction at exit is found. This is seen in figure 9, plate 15, where a cross-section taken through the minimum film thickness is shown. This confirms the supposition of Bennett & Ettles (1968) that such constrictions do exist in thrust bearings.

PHILOSOPHICAL TRANSACTIONS OF THE ROYAL SOCIETY A MATHEMATICAL, PHYSICAL & ENGINEERING SCIENCES

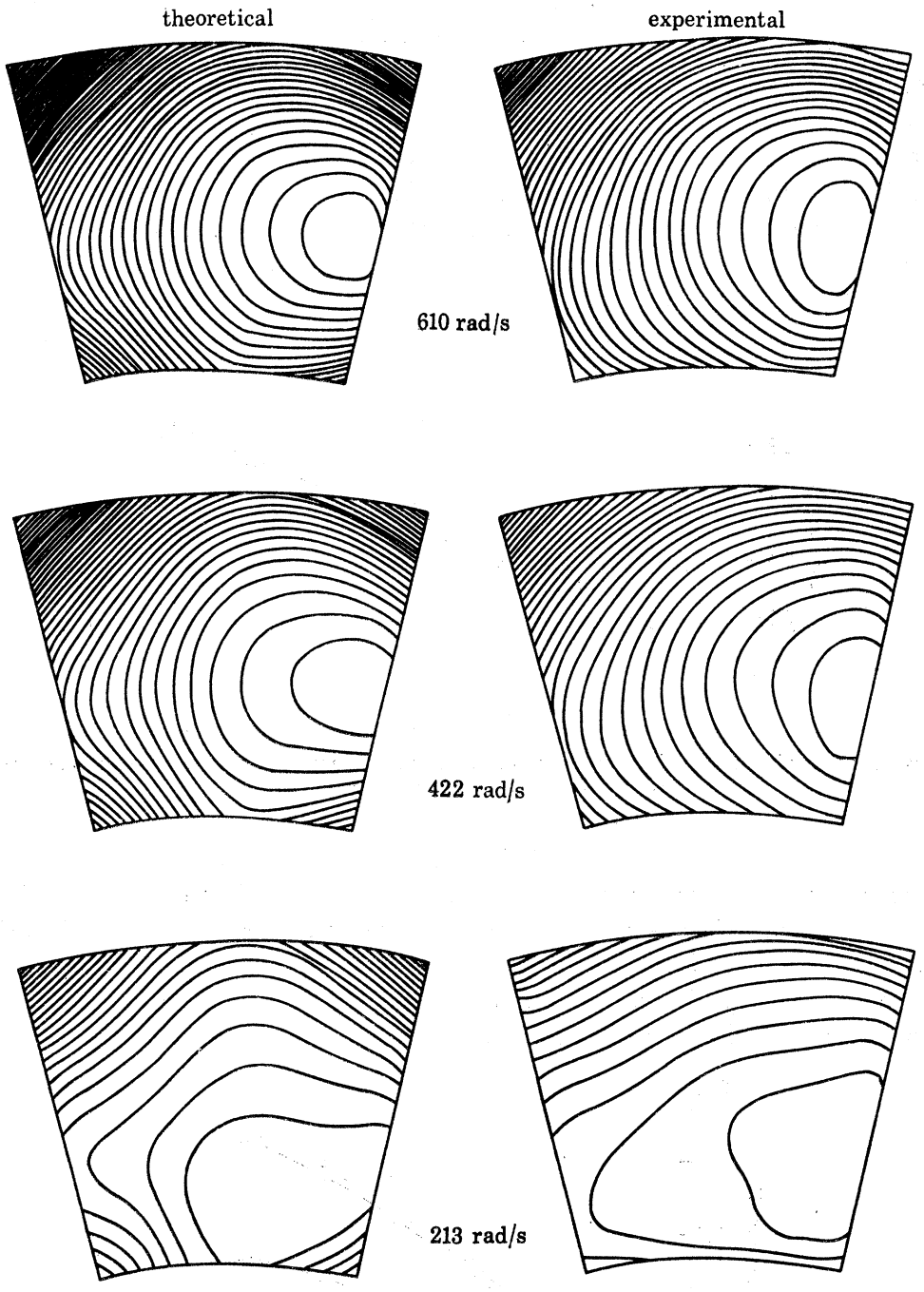

FIGURE 8*b*. Comparison of experimental and theoretical film shapes.
(*a*) Load 1.37 MN/m²; (*b*) load 6.89 MN/m².

Minimum film thickness

The values of minimum film thickness calculated from the hydrodynamic theory described in the first part are plotted non-dimensionally as h_0/B against $(\eta U/p_s B)^{\frac{1}{2}}$ in figure 10. These results are compared with experimental data collected by Kettleborough *et al.* (1955) who tested a 100 mm diameter centrally pivoted bearing of very similar geometry. The results show surprisingly good agreement and support the hydrodynamic theory.

Pressure distribution

The pressure distributions calculated for all test conditions were all almost symmetrical and parabolic. If it were truly parabolic the peak pressure p would be $\frac{9}{4}$ times p_s the specific pressure. The percentage difference between p and $\frac{9}{4}p_s$ was calculated and found to increase slightly with both speed and load. To within 1 % this could be expressed as percentage difference $= 2.77 \times 10^{-3} Np_s$, where N is the speed in rad/s and p_s is the specific pad pressure in MN/m².

Further the centre of pressure and the peak pressure very nearly coincided for all cases.

These findings are of value as once a simple pressure profile can be assumed the Reynolds equation can be reduced to a much more simple form and the computing reduced considerably.

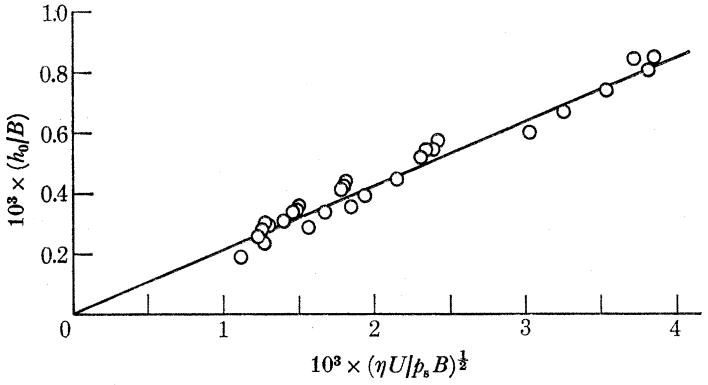

FIGURE 10. Plot of minimum film thickness h_0/B against load parameter $(\eta U/p_s B)^{\frac{1}{2}}$ with experimental results (——) of Kettleborough *et al.* (1955).

Film temperature

Temperature is one of the most important factors in lubrication. It is also one of the hardest to calculate and measure. The values calculated and measured here agree extremely well as the graphs of figures 11, 12 and 13 show. By using the theory derived above and using *only* the pad inlet temperature measured at the groove, the pad outlet temperature can be calculated. This agrees extremely well with the measured values.

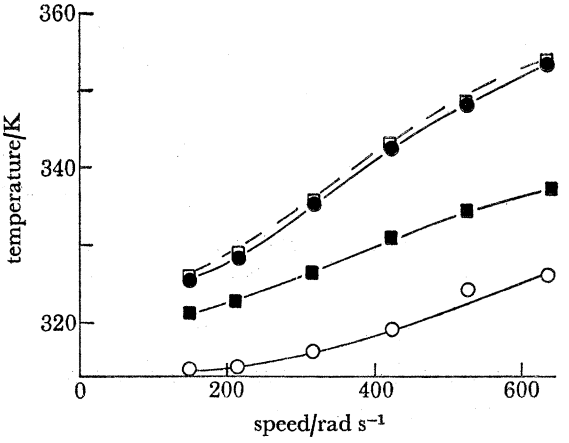

FIGURE 11. Plot of bearing temperatures against speed at 1.37 MN/m² specific load. ○, Bulk oil temperature in bearing housing; ■, average pad inlet temperature; ●, average paid outlet temperature, measured; □, average pad outlet temperature, calculated.

The important finding is that providing conduction *through* the pad is taken into account the agreement is excellent. If the system is considered adiabatic, i.e. no heat escapes through the pad by conduction, the calculated values are far too high. As an example, at the highest load and speed 6.89 MN/m², 628 rad/s the error is only 7 K including conduction but 60 K neglecting it.

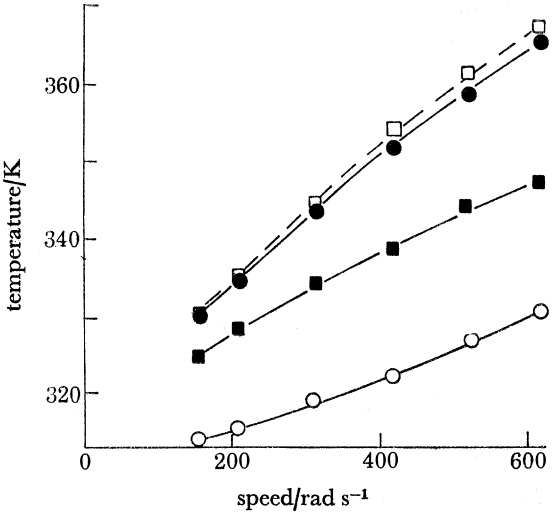

FIGURE 12. Plot of bearing temperatures against speed at 4.14 MN/m². See figure 11 for key to symbols.

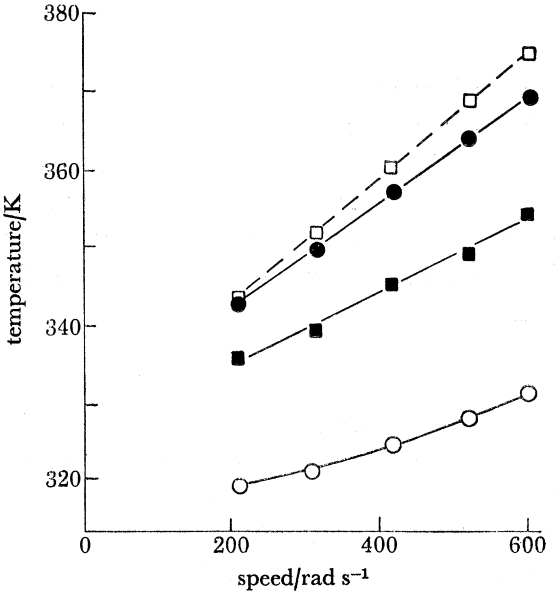

FIGURE 13. Plot of bearing temperatures against speed at 6.89 MN/m² specific load.
See figure 11 for key to symbols.

Heat balance

In the analysis described in part I the temperature through the thickness of the films is considered constant. Consider the case of a one-dimensional bearing where the temperature rise from inlet to outlet is linear and equal to ΔT and at a rough approximation the film thickness ratio inlet/outlet is 2. Previous analysis of pressure distribution has shown the position of zero

pressure gradient to be at the centre of the pad. The volume flow rate of oil per unit width is, therefore, $0.75Uh_0$ giving a convected heat flow per unit width of $0.75\sigma\rho Uh_0\Delta T$. It may be noted from figures 11–13 that the pad inlet temperature is approximately midway between the pad backing or groove temperature and the pad exit temperature. This will cause a conductive heat flow through the pad of $(kB/t)\,\frac{3}{2}\Delta T$ per unit width. A rough approximation to the ratio convected/conducted heat is, therefore, $\frac{1}{2}\sigma\rho Uh_0 t/kB$.

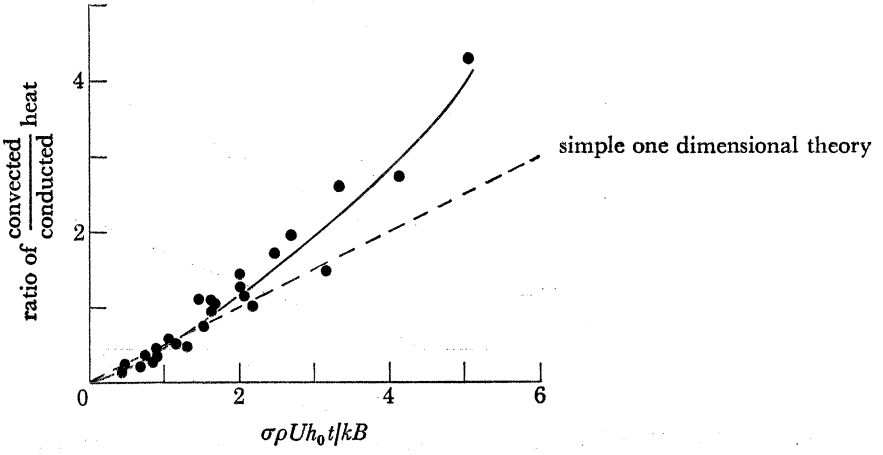

FIGURE 14. Ratio convected/conducted heat plotted against the parameter $(\sigma\rho/k)\,(Uh_0 t/B)$.

By integrating the appropriate heat terms of the energy equation over the pad area using measured temperatures and film shapes, and the calculated minimum film thickness values this ratio is plotted as a function of $\sigma\rho Uh_0 t/kB$ in figure 14. The curve agrees well with the simple theory at low speed or high loads, but the error increases as the speed increases and load reduces. The important finding here is that conduction is the major mode of heat transfer at low speeds and high loads, a point which is not made clear in current literature. The higher the speed and lower the load, the less becomes the effect of conduction.

Calculated and measured distortion

The distortions calculated from part I are compared with theory. Distortion in this context means departure from flatness. Longitudinal and transverse distortions defined in figure 15 are shown for the heaviest load (6.89 MN/m²) over a range of speeds and for two speeds (209 and 628 rad/s) over a range of loads in figures 16 *a* and *b*.

The general trend that distortion increases with speed is expected, due to the increasing temperature difference across the pad and so greater thermal movement. The transverse distortion is greater than longitudinal (in the direction of motion). The major shortcoming in the theory at high loads and low speeds is that elastohydrodynamic effects shown in figure 9 are not included. These, though identified, were not included due simply to the enormous extra complexity and length of the programme necessary for their treatment. The technique for doing this has been published a number of times, see, for example, Dowson & Higginson (1959).

With load, two modes are in opposition. Bending increases with load but so does direct compression and the two tend to cancel out, hence the relatively flat load/distortion curve.

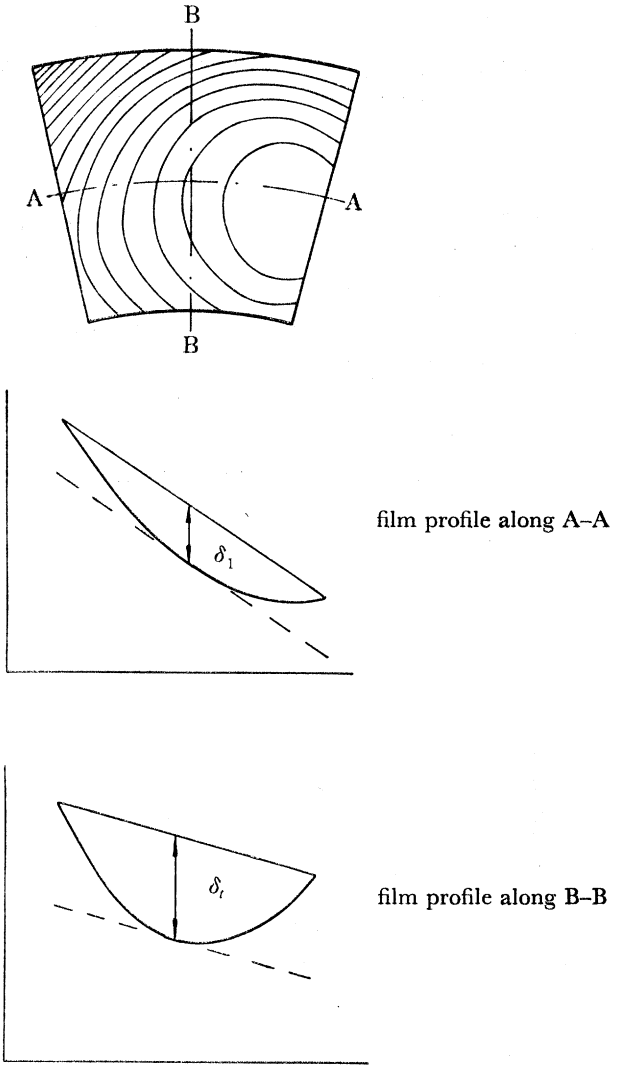

FIGURE 15. Definition of longitudinal and transverse distortion.

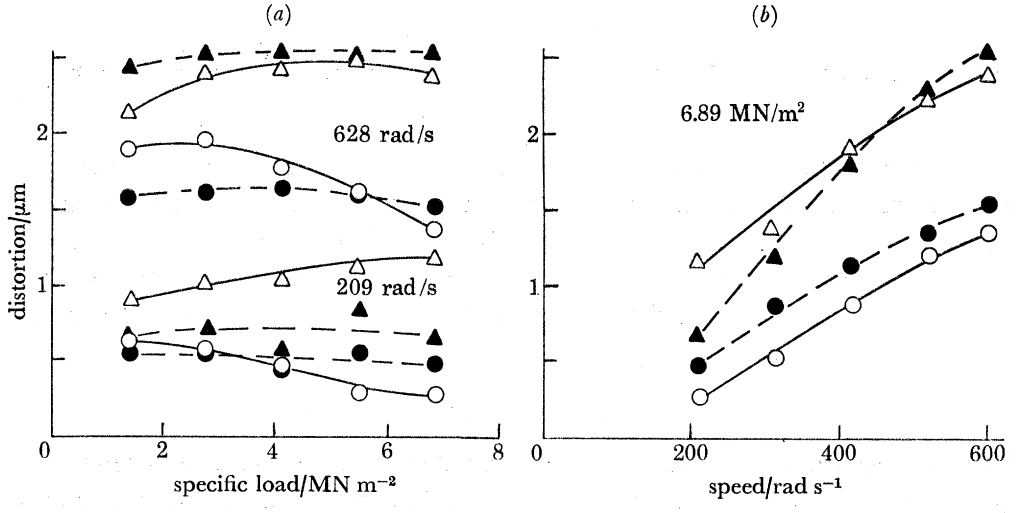

FIGURE 16. Measured and theoretical distortions for (*a*) 209 and 628 rad/s over a range of loads, (*b*) 6.89 MN/m² load over a range of speeds. ○, Longitudinal, measured; ●, longitudinal, calculated; △, transverse, measured; ▲, transverse, calculated.

The results displayed in figure 16 show that there is reasonable agreement between experiment and theory. It is a tribute to the power of the interferometric method that such small variations across the pad can be assessed so accurately. No other method is capable of this.

Load capacity

The classical Michell theory predicts that pads with central pivots will not carry any load at all. The entire work presented here concerns itself with the load actually carried by such pads. The cause being, of course, that pads deflect thermally and elastically and this gives the necessary asymmetry. This deformation load carrying process was analysed ingeniously by Raimondi (1960) who solved Reynolds equation for a centrally pivoted square pad and assuming the distortion caused the plane surface to become spherical. The viscosity he took as being constant.

Martin (1970) suggested plotting these results in the form $h_0(p_s/\eta UB)^{\frac{1}{2}}$, which is the square root of load capacity, against $\delta(p_s/\eta UB)^{\frac{1}{2}}$, or dimensionless distortion.

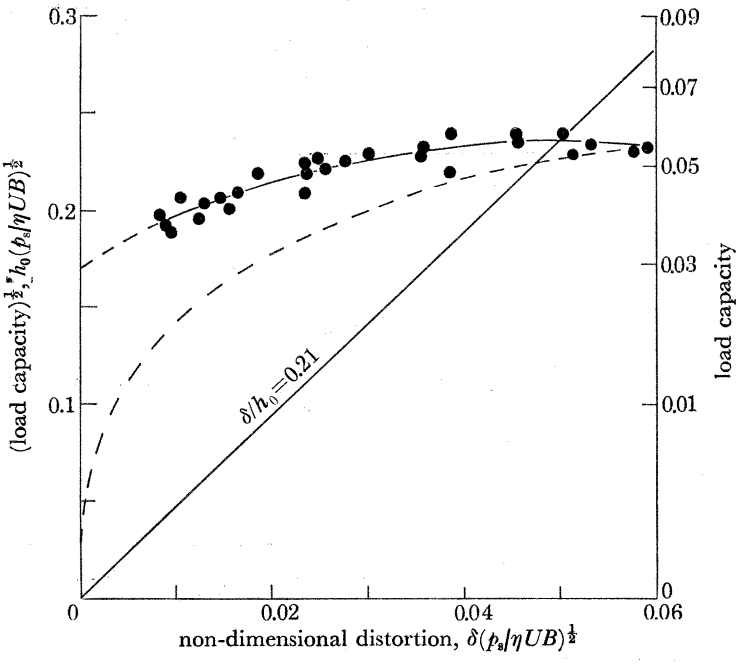

FIGURE 17. (Load capacity)$^{\frac{1}{2}}$, $h_0(p_s/\eta UB)^{\frac{1}{2}}$ plotted against distortion parameter $\delta(p_s/\eta UB)^{\frac{1}{2}}$. (— — —, Raimondi.)

The experimental data are given in figure 17, with the results from Raimondi's theory. Once more theory predicts zero load capacity at zero distortion, whereas the experimental data suggests that $h_0(p_s/\eta UB)^{\frac{1}{2}}$ is 0.17. The reason for this is that viscosity variation moves the centre of pressure towards the pad centre which gives a sizeable load for a flat pad, an effect not observed when constant viscosity is assumed. Figure 17 also shows that load capacity is at a maximum when the distortion is 0.21 times the minimum film thickness.

Full theoretical analysis

The full computer program described in the first paper gives a simultaneous solution to the governing Reynolds, energy and elastic–thermal distortion equations. This was run in only four cases owing to the amount of computer time needed.

The more approximate theory used to date simplified the full treatment by using the film shape as measured by the interference method.

The results are displayed in table 4. The first column is the computed minimum film thickness based on *measured* film shape and temperatures. The limitation of the monochromatic interference method is that it only gives differences of thickness, not absolute values. The removal of this restriction is our next task. This explains why the minimum film thickness in column 1 can only be *computed* from other measured data. In column 2 the full computer solution is given and in column 3 the computer solution neglecting distortion is listed.

The differences between the first two are slight. Minimum film thicknesses are within 3% except for the high load–low speed case, which is 8% in error due to the neglect of e.h.l. distortion. Average outlet temperatures agree to within 4.5 K and maximum film temperature to within 6.3 K.

The most striking differences are apparent in the solutions *neglecting* distortion. Film thicknesses are up to 40% too low and corresponding maximum film temperatures 32 K too high.

TABLE 4. COMPARISON OF RESULTS

test condition	property	1 calculated from measurements	2 computed	3 computed neglecting distortion
211 rad/s	minimum film thickness/μm	12.27	12.59	7.16
1.37 MN/m²	maximum film temperature/K	330.28	332.60	340.39
	average outlet temperature/K	328.70	327.52	332.99
644 rad/s	minimum film thickness/μm	15.45	15.60	12.07
1.37 MN/m²	maximum film temperature/K	356.44	353.46	370.84
	average outlet temperature/K	351.34	349.29	358.99
214 rad/s	minimum film thickness/μm	3.30	3.56	2.85
6.89 MN/m²	maximum film temperature/K	344.43	347.64	361.96
	average outlet temperature/K	342.75	342.70	346.29
610 rad/s	minimum film thickness/μm	5.39	5.54	3.90
6.89 MN/m²	maximum film temperature/K	376.40	382.61	414.55
	average outlet temperature/K	369.73	374.10	389.78

CONCLUSIONS

The aim of this research has been to extend the use of interferometry to thrust bearings, its use being well known for point contact studies. Interferograms give a detailed mapping of the film shape which allows exact analysis of its operation if the governing equations can be solved. The comparison of the measured and computed results is encouraging and one may conclude that the two agree. The assumption made in the theoretical section, all concerning temperature, seem to be valid. These assumptions are broadly

(1) The temperature of the lubricant is constant through the *thickness* of the film.

(2) The temperature at the back of the pad surface is constant and equal to that of the inlet oil.

(3) The temperature gradient through the pad is linear.

A most important conclusion is that distortion contributes very markedly to the operation of the pad. Thermal distortion is about double that of elastic and furthermore, is far more complex to determine as the number of assumptions necessary to obtain *any* solution makes plain. Neglect of distortion gives unreliable results. The action of heat on viscosity is normally considered

PHILOSOPHICAL TRANSACTIONS OF THE ROYAL SOCIETY A MATHEMATICAL, PHYSICAL & ENGINEERING SCIENCES

deleterious to load carrying capacity. For centrally pivoted pads it *increases* the load carrying capacity at low values of the distortion number, by moving the centre of pressure to the middle of the pad.

The two main conclusions from this work are, therefore

(1) The use of interferometry can be extended to bearings of this type and give a detailed map of the whole field.

(2) The governing equations can be solved and give excellent correlation with measured values even with the assumptions needed to make them tractable.

References

Bennett, A. H. & Ettles, C. M. M. 1968 *Inst. Mech. Engrs Tribology Convention, London* paper 17, p. 139.
Born, M. & Wolf, E. 1965 *Principles of optics*. Pergamon Press.
Dowson, D. & Higginson, C. R. 1959 *J. Mech. Engng Sci.* **1**, 6–9.
Françon, M. 1966 *Optical interferometry*. New York: Academic Press.
Kettleborough *et al.* 1955 *Proc. I. Mech. E.* **169**, 746.
Martin, F. A. 1970 *Tribology Convention. London. Inst. Mech. Engrs*, paper 16, p. 120.
Munro, D. M. 1967 A Fortran IV contour mapping program. Engineering in Medicine Laboratory, report no. 4. Imperial College.
Raimondi, A. A. 1960 *Trans. A.S.L.E.* **3**, 216.
Rippel, H. C. 1962 *Cast bronze hydrostatic bearing design manual*. Cleveland, Ohio: Cast Bronze Bearing Institute.

PHILOSOPHICAL TRANSACTIONS OF THE ROYAL SOCIETY A MATHEMATICAL, PHYSICAL & ENGINEERING SCIENCES

(*a*) 209 rad/s (*b*) 419 rad/s (*c*) 628 rad/s

FIGURE 6. Fringes from white metal pad at 2.76 MN/m² specific load.

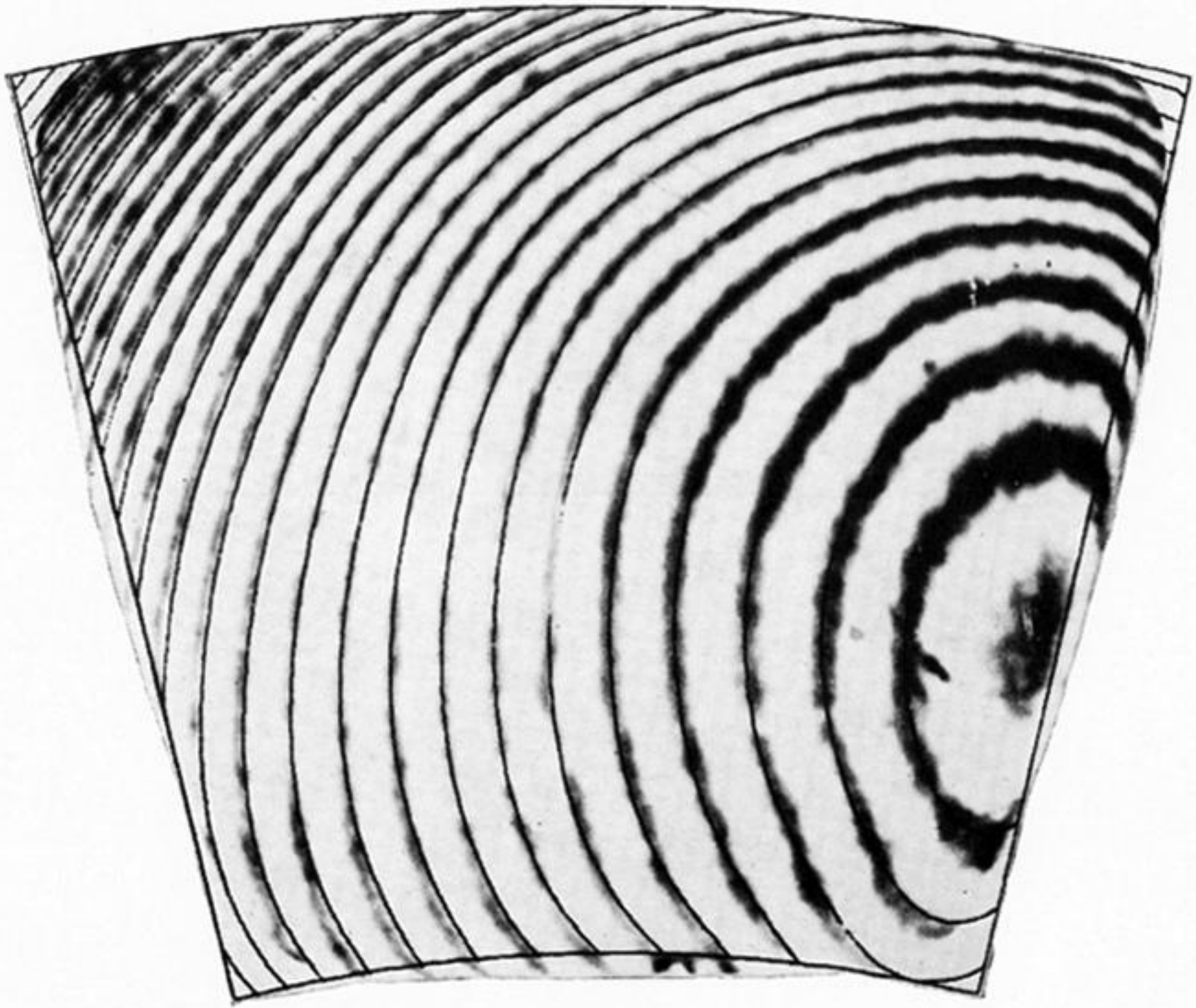

FIGURE 7. Typical interferogram with digital print out superimposed.

PHILOSOPHICAL TRANSACTIONS OF THE ROYAL SOCIETY A

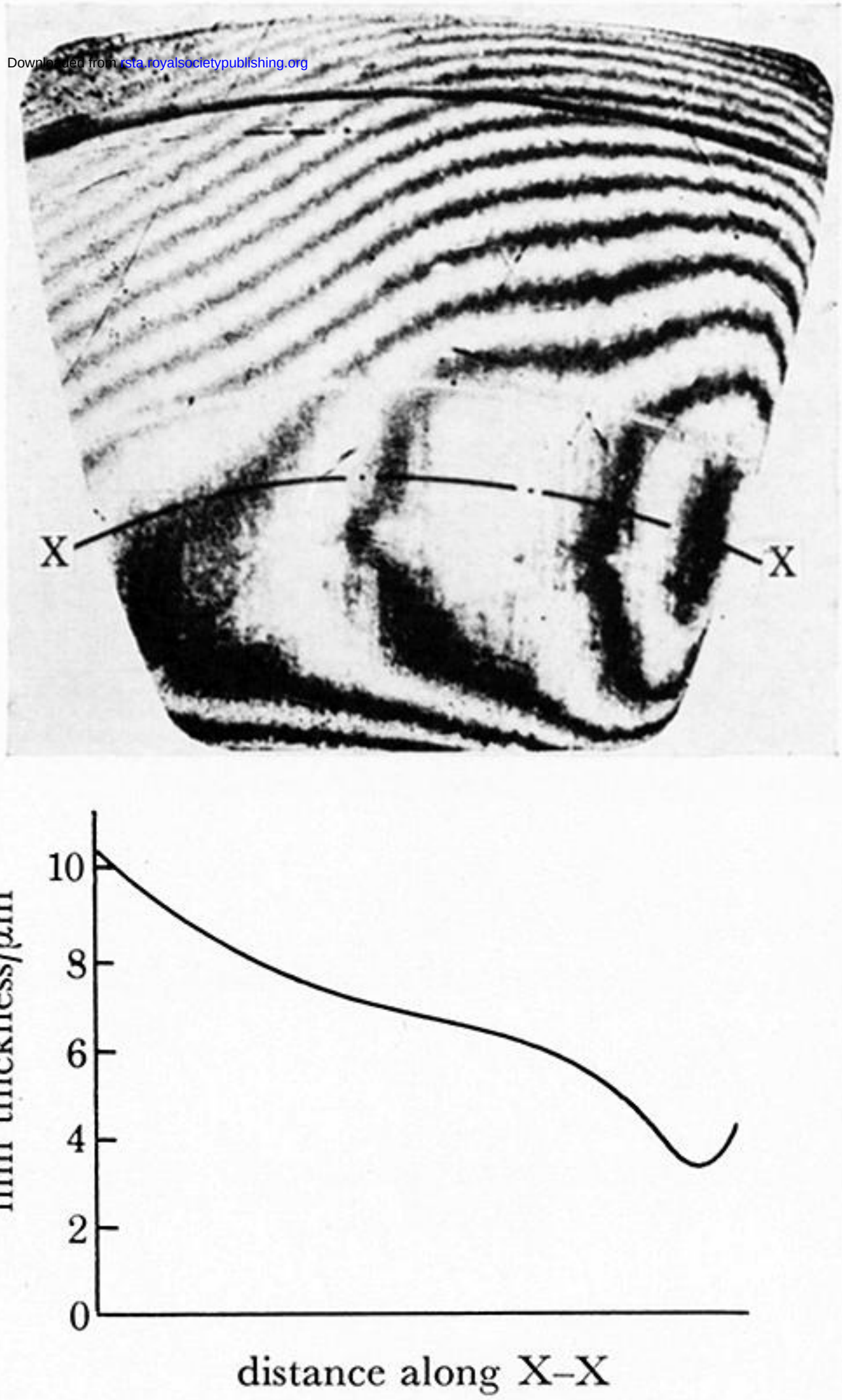

FIGURE 9. Interferogram and cross section showing ehl construction at exit.